Plasma Sources
Science and
Technology

Production of reactive species by using surface dielectric barrier discharge in direct contact with water

To cite this article: Oleksandr Galmiz *et al* 2025 *Plasma Sources Sci. Technol.* **34** 025011

OPEN ACCESS
IOP Publishing

Plasma Sources Science and Technology

Plasma Sources Sci. Technol. **34** (2025) 025011 (17pp)

https://doi.org/10.1088/1361-6595/adb3cb

Production of reactive species by using surface dielectric barrier discharge in direct contact with water

Oleksandr Galmiz*, Richard Cimerman, Pankaj Pareek,
Mário Janda and Zdenko Machala

Division of Environmental Physics, Faculty of Mathematics, Physics and Informatics, Comenius University in Bratislava, Mlynská dolina, 842 48 Bratislava, Slovakia

E-mail: oleksandr.galmiz@uniba.sk

Received 17 July 2024, revised 5 November 2024
Accepted for publication 7 February 2025
Published 20 February 2025

Abstract

Surface dielectric barrier discharge (SDBD) ignited directly from the liquid electrodes at the 3-phase gas/liquid/solid interface represents a novel approach in both water and polymer surface treatment methods. This study investigates the gaseous and liquid-phase reactive oxygen and nitrogen species (RONS) generated by this discharge. The impact of the discharge power and treatment duration on the concentration of these species in both gas and liquid is explored. The spatial development of ozone, the prevailing molecule produced by air dielectric barrier discharge, is studied. The production yields of plasma-generated species in the gas are described. Additionally, the electrical measurements of the SBDB with liquid electrode are presented and its characteristics are discussed. The combined investigation of RONS production yields, electrical discharge characterization, and *in-situ* ozone evolution provides important information regarding the presence of the reactive species in the vicinity of the plasma discharge, supporting further development and targeted applications of this technology.

Keywords: cold atmospheric plasma, liquid electrodes, plasma activated water (PAW), reactive oxygen and nitrogen species (RONS), surface dielectric barrier discharge (SDBD)

1. Introduction

Plasma-activated water (PAW) in general is a type of water that has been treated with plasma discharge and has shown potential use in numerous emerging applications. These applications of PAW include e.g. enhancement of seed germination, plant growth [1–3], selective treatment of cancer cells [4], wound healing [5, 6], food preservation [7, 8], inactivation of bacteria [9–11], viruses [12], pests [13], and fungi [14], *etc*.

The main reason for multiple PAW applications is the remarkable chemical activity of water (liquids) after being in contact with non-equilibrium plasma. It is now well known that electrical discharges in liquids and in the gas phase over the liquid surface generate a diversity of reactive oxygen species (ROS) and reactive nitrogen species (RNS) such as radicals, ions, excited atoms, and molecules (e.g. ·O, ·OH, H_2O_2, O_3, N_2^-, O_2^-, etc). These reactive species are capable of decomposing organic pollutants and killing microorganisms at atmospheric pressure and ambient temperature [15, 16].

The above-mentioned reactive oxygen and nitrogen species (RONS) are formed in PAW due to the transport of gaseous species and radicals generated by the plasma in the vicinity of the plasma–water interface. The formation of RONS results

---

[*] Author to whom any correspondence should be addressed.

in changing the physicochemical properties of PAW, such as pH, oxidation-reduction potential, total dissolved solids, and electrical conductivity [17], which in turn changes the plasma parameters and its effects.

A comprehensive review by Lu *et al* gives the most important mechanisms for generating and transporting ROS, RNS, and other species from the non-equilibrium atmospheric pressure plasmas to the liquid medium [18]. They discuss applications of RONS in plasma medicine, hygiene, and other fields. In general, plasma treatment of water-based liquids leads to the formation of various RONS, which strongly depend on the reactor configuration and applied operating parameters, as well as the chemical composition of the gas and liquid. This enables tailoring the most favorable conditions for each studied PAW formation process in terms of desired effects and energy efficiency.

Various kinds of plasma sources have been used to produce RONS in PAW. The plasma reactors can be categorized by either indirect contact or direct contact with liquid. In the former, the treated liquid does not form a part of the discharge electrical circuit, but the plasma is sufficiently close to allow species interaction and transport. In the latter, including the one presented in this study, plasmas directly interact with aqueous liquids.

Plasma jets are the most commonly used non-equilibrium plasma sources [19–26], but many other studies use, for example, pin-to-plane (or water) corona or spark discharge [27–29], pin-in-water discharge with gas bubbling [30, 31], gliding arc discharge [29, 32, 33], dielectric barrier discharge (DBD) [10, 34–39] and others [40].

The DBD is characterized by the presence of a dielectric material in between electrodes in various configurations [41, 42]. Such configurations could be subdivided into volume DBD and surface DBD. Typically, surface DBD is more efficient than conventional volume DBD [43, 44].

Particularly surface DBD (SDBD) has become a focal point of extensive research due to its versatile applications in surface treatments, bio-decontamination, plasma medicine, and treatments of biological fluids and water. It is used as a plasma-based chemical reactor in many environmental applications, such as ozone production, NO_x conversion, decomposition of volatile organic compounds, removal of organic pollutants from water, inactivation of microorganisms, and killing bacteria [43–54].

Ozone is considered to be the most important reactive species generated in the SDBD configuration for environmental applications, especially for water treatment, due to its high oxidization ability.

Usually, the SDBD plasma is generated in a thin layer along the dielectric surface. A drawback of SDBD for water treatment is that it does not reach the treated water. This results in a steep decrease in the concentration of short-lifetime reactive species with high oxidation potentials, such as ·OH and ·O radicals, in the water.

The configuration that was used in this study addresses previous limitations by utilizing liquids as electrodes, allowing the SDBD to ignite directly from the liquid surface [48, 49, 55, 56]. Though the area of contact with the liquid is limited to the perimeter of the dielectric tube that is used, such a system could be scalable and modified according to the specific needs. Moreover, besides water activation with RONS, this approach supports surface treatment and cleaning of dielectric tube materials, with potential applications in material processing and medicine. Altogether, these findings can drive further development and facilitate the targeted use of this technology.

In the present work, we investigated the formation of reactive species, such as H_2O_2, O_3, NO_2^-, and NO_3^-, generated by a new type of SDBD in tap water utilizing UV–VIS absorption spectroscopy. The Fourier transform infrared (FTIR) absorption spectroscopy measurements were performed to obtain information on the concentrations and production yields of plasma-generated species in the gas. The UV–VIS *in-situ* absorption spectroscopy data showing the spatial evolution of O_3 are also presented.

In addition, the mechanism of the RONS production processes is discussed. We evaluated the efficiency of the SDBD for ozone and nitrogen oxides synthesis, which unravels for the first time the performance of such an SDBD system for nitrogen oxides and ozone production.

2. Experimental setup

In order to simulate the triple-phase interface (plasma–liquid–solid) under stable conditions, a thin glass test tube with a diameter of 10 mm and a wall thickness of 0.5 mm, filled with tap water (electrical conductivity ~0.3 mS cm^{-1}) and surrounded by atmospheric air, was used. The liquid inside the test tube was connected to the high-voltage (HV) power supply generating a sine voltage waveform. The test tube was positioned in the middle of the Petri dish filled with the grounded liquid. Both electrically insulated solutions (inside and outside the test tube) served as liquid electrodes as depicted in figure 1. A more detailed explanation of the discharge could be found in [49, 56] where a similar principle of the discharge was used.

The SDBD discharge was operated in the ambient air at atmospheric pressure. The HV sine waveform was set to the amplitude of 0–20 kV and operated at a frequency of approximately 31 kHz. The power to the liquid electrodes was supplied by a HV resonance generator *Lifetech-300 W* coupled with a function generator. The electrical characteristics of the discharge were monitored using an HV probe (*Tektronix P6015A*) and current monitor (*Pearson Electronics 4100*), both connected to a digital oscilloscope (*Tektronix TBS 2104*, 100 MHz, 1 GSa s^{-1}). Discharge power was calculated using the Lissajous figure method, with an additional 10 nF series capacitor added to the circuit for these measurements.

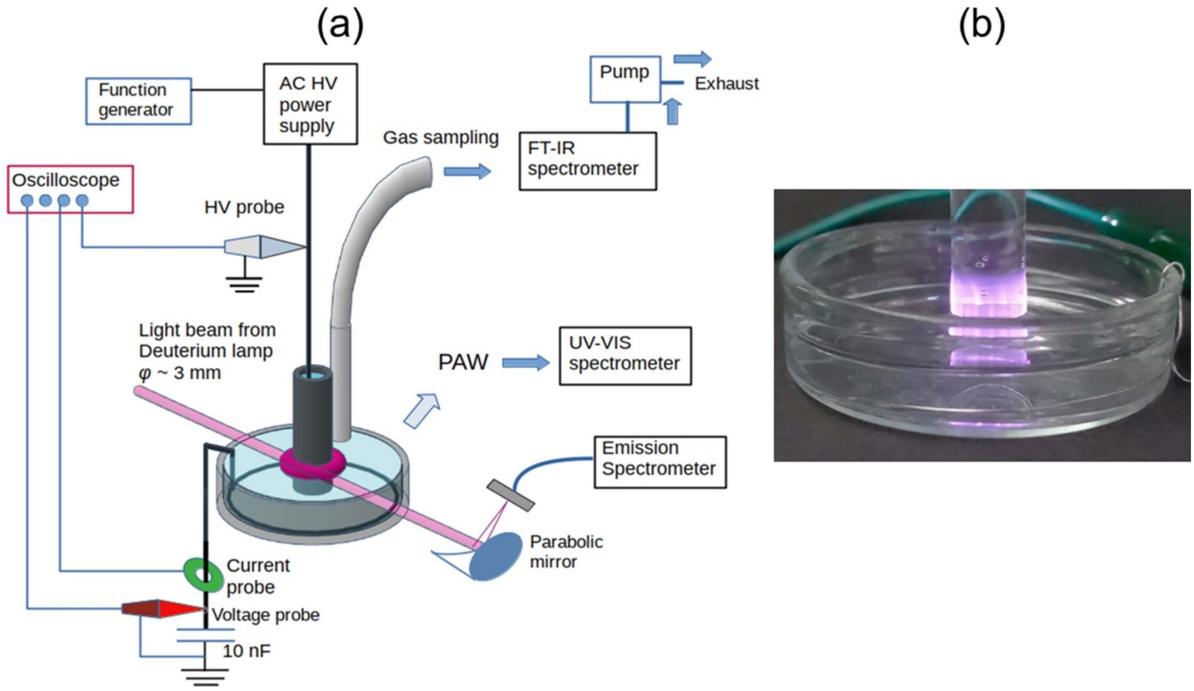

Figure 1. Schematic of the experimental assembly for the SDBD treatment of water around the glass tube with the *in-situ* UV–VIS absorption diagnostics (a) and the discharge photo taken at the discharge power of 10 W (b).

2.1. Current pulse measurements

The single-shot current waveforms were recorded by a digital oscilloscope using a sample rate of 250 MS s^{-1} which corresponds to the sample interval of 4 ns between two adjacent data points. A statistical analysis of the recorded current pulses was then performed and histograms of the amplitudes of current pulses were calculated using our home-developed computer program. A more detailed explanation of the program algorithm can be found in [57]. The amplitudes of the pulses were evaluated as vertical distances from the calculated baseline that represents the capacitive component of the current (figure 2). Histograms of the current pulse amplitudes were then generated with 5 mA bin intervals, setting a 10 mA minimum threshold to filter out the noise. The data in these histograms represent averages from ten recordings, and the average pulse amplitude was calculated from these histograms. Error bars were calculated as standard deviations. While this method may underestimate some microdischarges due to the height threshold parameter, it provides representative data.

2.2. Gas analysis

The analyzed gas was pumped through a gas tube (PTFE, 6/4 mm) placed 1 cm above the grounded liquid electrode by the air pump with a constant flow rate of 1.3 l $\min^{-1}$. The air flow rate determines the gas mixing and accumulation of gaseous species produced by the plasma and, therefore, has a big impact on the plasma chemistry in the gas phase and consequently in the aqueous phase [58]. During the measurements, the air flow rate was chosen as a compromise between the time needed for filling the gas cell and the detection limit of the species.

Typically, the humidity in the vicinity of the plasma is elevated due to the water heating by the plasma effects. During the measurements, the relative humidity was measured by placing the sensor (*Arduino*) as close to the plasma as possible. Still, the distance between the sensor and the plasma was approximately 5 mm with slight variations based on the input voltage. The maximum recorded relative humidity was 65%.

2.2.1. Fourier transform infrared (FTIR) spectroscopy. The chemical analysis of gaseous species produced by the SDBD was performed by FTIR absorption spectroscopy (*Shimadzu IRSpirit-X* spectrometer) using a 542 cm absorption path gas cell equipped with ZnSe windows. The spectra measurement was carried out in the infrared region of 4000–500 cm^{-1} with a resolution of 0.9 cm^{-1}. The FTIR spectra allowed the identification of gaseous species (ozone O_3, nitrous oxide N_2O, dinitrogen pentoxide N_2O_5) generated by SDBD discharge. The following absorption bands were used to evaluate the concentrations of detected gaseous species: O_3 at 1055 and 2120 cm^{-1}, N_2O at 2235 cm^{-1}, and N_2O_5 at 742 and 1245 cm^{-1}. The concentrations of the gaseous species were evaluated in absolute (ppm) units by modeling the absorption spectra of each species using a set of absorption lines from the HITRAN database (more details can be found in [59]).

In addition to the concentration of the gaseous species, the production yield PY (i.e. the amount of produced gaseous species per energy density ED) of the species was also calculated as follows:

$$\mathrm{PY} = \frac{c}{\mathrm{ED}} = \frac{Q * c}{P} \tag{1}$$

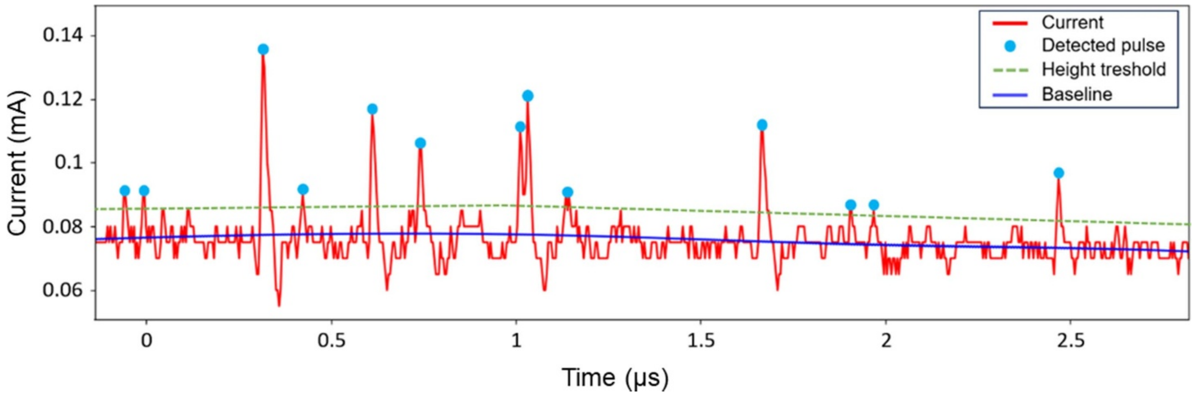

Figure 2. Detail of a recorded current waveform with the marked baseline and height threshold.

where *Q* represents the air flow rate, *P* is the discharge power, and *c* represents the concentration of gaseous species produced by the discharge.

2.2.2. In-situ O_3 *detection by UV–VIS absorption technique.*

To determine spatial distributions of reactive species concentrations around the glass tube inserted in the treated water in the reactor, the *in-situ* measurements using the UV–VIS absorption spectroscopic technique were performed (figure 1(a)).

As a light source, deuterium lamp *Avantes AvaLight-D-S* was used, with the spectrometer *Avantes AvaSpec-Mini4096 CL* for spectrally resolved light detection. Spectra in the range 190–650 nm with the spectral resolution is 0.4–0.5 nm were recorded.

Radiation from a deuterium lamp was reflected by a parabolic mirror, which turned it into a parallel beam (diameter ~3 mm, limited by an iris diaphragm) that traveled across the reactor above the treated water surface in the vicinity of the glass tube inserted in the treated water. The distance of the beam from the water surface was varied starting from the triple-phase point (liquid/solid/gas), up to a maximum distance of 2.5 cm. The spatial step during the measurements was 0.5 cm.

At the other side of the reactor, the transmitted part of the radiation was focused by another parabolic mirror to the optical fiber connected to the entrance slit of the spectrometer. By comparing the spectrum measured with the plasma on and off, we determined the ozone concentration by fitting the measured spectra with the synthetic spectra calculated for the 2 mm absorption path. The UV–VIS absorption cross-section of O_3 was downloaded from the MPI-Mainz UV/VIS Spectral Atlas [60]. Due to relatively high detection limits (~10 ppm), concentrations of RNS (NO, NO_2, and HNO_2) could not be detected and quantified.

2.3. *Water analysis*

Plasma–water interactions involve hundreds of various species and thousands of reactions in both gas and liquid phases. Nevertheless, there are some common products and methods of quantification that are helpful when characterizing the chemical changes in the water treated [61].

The discharge interacting with water solutions facilitates an effective transfer of plasma-generated gaseous reactive species. With the help of UV–VIS absorption spectroscopy (*Shimadzu UV-1800*) the main aqueous species such as hydrogen peroxide H_2O_2, nitrite NO_2^- and nitrate NO_3^- were detected and their absolute concentrations were evaluated.

The detection of the dissolved ozone was performed by the indigo blue assay. It is a simple and quantitative colorimetric standardized method for ozone detection in water and wastewater [62]. In acidic conditions, O_3 rapidly decolorizes the indigo potassium trisulfonate dye and the colorless product isatin is formed by the bleaching process. The decrease of the absorbance at 600 nm ($\varepsilon = 2.38 \times 10^4$ M^{-1} cm^{-1}) is linear with the increasing concentration of the dissolved O_3. However, it should be noted that this method may not be perfectly specific enough for O_3. It was previously shown that it may cross-correlate, especially with ·OH radicals or other ROS in the PAW [63]. Therefore, the indigo blue assay that was used to detect $O_{3(aq)}$ might have overestimated the real $O_{3(aq)}$ concentration.

The concentration of H_2O_2 was evaluated by titanium oxysulfate $TiOSO_4$ assay under acidic conditions [9, 16, 64]. The reaction of titanyl ions Ti^{4+} with H_2O_2 leads to the formation of a yellow-colored complex of pertitanic acid H_2TiO_4 with an absorption maximum at 407 nm. The color intensity is proportional to the H_2O_2 concentration. To prevent the H_2O_2 decomposition by the reaction with NO_2^- under acidic conditions, after the discharge treatment, the sample was immediately stabilized by 60 mM sodium azide NaN_3 solution. Sodium azide reduces NO_2^- into molecular N_2 and preserves the H_2O_2 concentration intact [16]. The used volume ratio of sample:NaN_3:$TiOSO_4$ was 10:1:5.

Concentrations of NO_2^- were evaluated by Griess reagents under acidic conditions [65, 66] using the chemicals and according to the protocol (Cayman Chemicals Nitrate/Nitrite Colorimetric Assay Kit # 780001). This method is easy to perform and approved as precise for $NO_x{}^-$ measurement in the PAW produced by plasma discharge [63]. The reaction of nitrites (NO_2^-) with the Griess reagents leads to the formation of a deep purple azo compound with an absorption maximum of 540 nm.

The total $NO_x{}^-$ concentration was evaluated by using 10 mM 2,6-xylenol and acid mixture (H_2SO_4:H_3PO_4 as 1:1) as the reagent. The 10 mM xylenol mixture was prepared by adding 122.16 mg 2,6-xylenol to 100 ml of 10% glacial acetic acid. The used volume ratio of sample:acid:xylenol was 1:8:1. The absorption maximum was recorded between 290 nm and 350 nm after subtracting the control in this region. The maximum peak is directly proportional to the concentration of $NO_x{}^-$. If the concentration of $NO_x{}^-$ was too high, we diluted the sample with deionized water to adjust the $NO_x{}^-$ concentration in the linear absorbance range. Finally, the NO_3^- concentration was obtained by subtracting the previously measured NO_2^- concentration from the $NO_x{}^-$ concentration [66, 67].

The so-called Iodine-starch test based on potassium iodide with starch was chosen to visualize ROS propagation during the plasma presence. The iodine-starch test is a chemical reaction of amylose, present in a common kitchen starch, with triiodide anions I_3^-. The potassium salt (KI) was used as the source of atomic iodine for the color indicator. Amylose itself does not react with the KI molecule, and the presence of an oxidizing agent is required, such as ROS particles generated in the plasma. The reagent contains 0.3% potassium iodide and 0.5% starch. Because the oxidation potential of I_2 is approximately 0.54 V, it can detect several ROS with oxidation potentials >0.54 V. Therefore, ·OH (oxidation potential 2.80 V), O (2.42 V), O_3 (2.07 V), H_2O_2 (1.78 V), and HO_2 (1.70 V) can be detected by this reagent [68].

3. Results and discussion

3.1. Electrical characterization of the SDBD

The acquired voltage and current discharge waveforms are depicted in figure 3(a). It can be seen that the current has two components: the first one (sinusoidal) is the displacement current component flowing through the electrode capacitance. The second component is a series of narrow pulses which appears in each half cycle of the applied voltage starting at the onset value and ending at the peak voltage value. Such an appearance is typical for the discharge operation in ambient air.

Figure 3(a) indicates that the discharge is ignited in the reactor in the form of filamentary streamers, which spread on the surface of the dielectric barrier accompanied by charging of the dielectric barrier and formation of streamer current pulses.

The high frequency of the emerging filaments results in a diffuse-like discharge appearance. With an increase in discharge power, the discharge becomes more intense and increases its area. While maintaining its overall visual characteristics, some of the most prominent filaments could be seen. Concurrently, as the discharge power rises, so does the discharge current. The Lissajous figure from which the discharge power was estimated is presented in figure 3(b).

The positive polarity half-cycle exhibits a higher amplitude of current pulses. This finding is consistent with the electrical characteristics of discharges observed in SDBD actuators [69] and similar studies [70, 71].

It is known, that the structure of the positive surface discharges resembles a pronounced tree-like structure with relatively homogeneous light emission intensity along its span. The discharge mechanism of positive surface discharges is of a streamer nature and no significant transition to the leader discharge takes place in our case. For negative surface discharges, the diffuse structure resembles a cometary shape. The small number of peaks in the current waveform during the negative polarity suggests, as noted by Akishev *et al* [72, 73], that there are practically no streamers present.

As can be seen from the current waveform presented in figure 3(a), the number of negative pulses is significant, however, most of these negative pulses have low amplitudes. The computer program that was used to evaluate the number of pulses intentionally filtered out pulses of low amplitudes so that signal noise would not erroneously contribute to the resulting pulse numbers. Thus, to avoid significantly biased results, an amplitude threshold was set to 10 mA (as mentioned in section 2.1) and the number of pulses with amplitudes below 10 mA has not been presented.

Figures 4(a) and (b) showcase histograms representing positive and negative current pulses, respectively, detailing the relationship between quantity and amplitude at a specific discharge power. These histograms, displayed with vertical logarithmic scales, provide a comprehensive view of pulse amplitude distribution during each half-period of the applied voltage. The analysis reveals that both, the number and amplitude distribution of pulses, are influenced by the discharge power and the polarity of the applied voltage. Noteworthy is the substantial increase in the average number of positive pulses exceeding 10 mA as the discharge power escalates. Specifically, the average number of such pulses surged from approximately 5 ± 1–37 ± 2 within the power range of 2.5 W to 15 W, indicating a pronounced correlation between discharge power and pulse quantity.

3.2. Gas phase analysis

The nonthermal plasma generated by atmospheric-pressure air discharges is characterized by a strong chemical activity. In the gas phase, discharges can produce various molecular species whose composition depends on multiple factors, such as the type of discharge, gas mixture, and discharge power [74]. One of the most abundant gaseous products of air discharges, in particular DBDs, is ozone O_3 [75, 76]. O_3 is principally produced by a three-body reaction of ·O atoms with O_2 molecules with the help of a third collision partner [75].

The production of O_3 by air DBDs is often accompanied by the production of nitrogen oxides NO_x. Out of them, nitrous oxide N_2O is one of the most frequent nitrogen-containing gaseous products. The N_2O production is primarily due to the reaction of the first excited state of molecular nitrogen $N_2(A)$ with O_2 molecules [77]. In addition to N_2O, nitric oxide NO can be also produced by the Zeldovich mechanism including the reactions of N_2 and O_2 with ·O and ·N species, respectively [78]. NO may be further oxidized by ·O or O_3 resulting in the

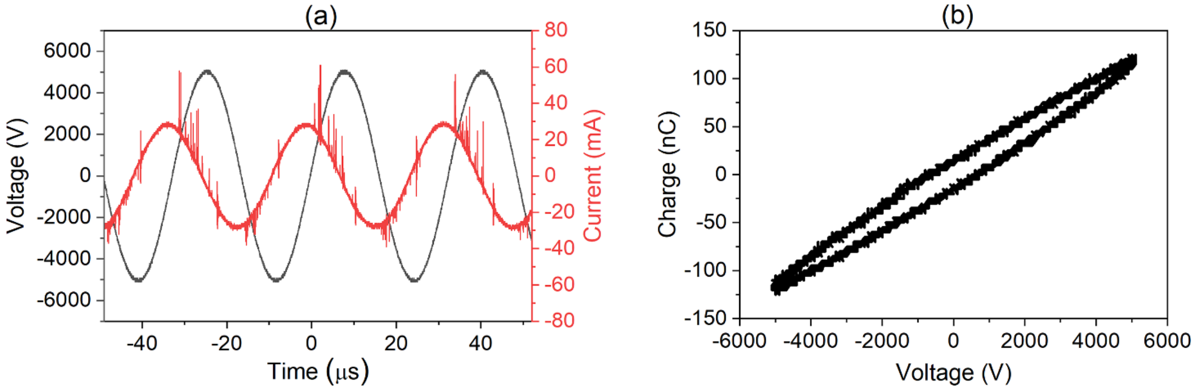

Figure 3. The typical voltage and current waveforms of the SDBD with liquid electrodes (a), and the obtained Lissajous figure (b).

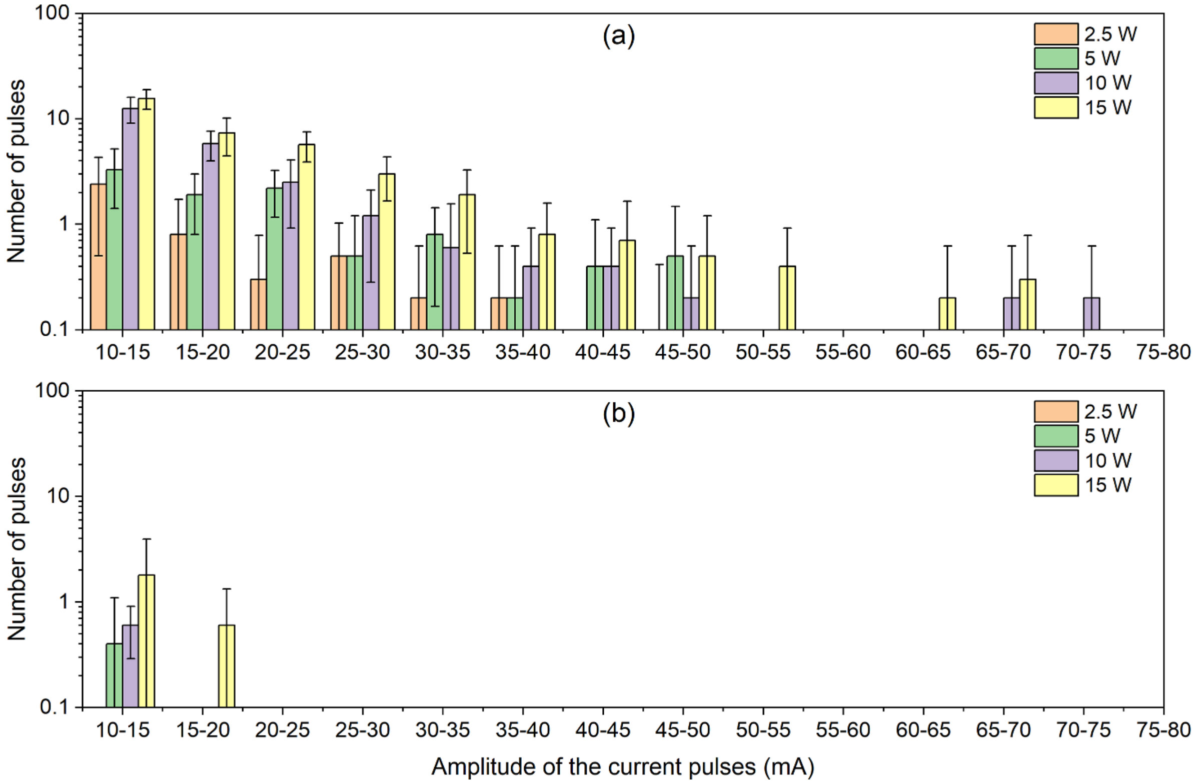

Figure 4. Histograms of amplitudes of positive (a) and negative (b) current pulses at various discharge powers.

production of nitrogen dioxide NO_2 [79]. NO and NO_2 may then contribute to the production of N_2O via reactions with excited nitrogen atom $N(^2D)$ or ·N species, respectively [80]. Moreover, in an oxidizing environment NO_2 can undergo further oxidation processes promoted by O_3 and ·O leading to the formation of dinitrogen pentoxide N_2O_5 [81]. In humid air-like mixtures, nitrous acid HNO_2 and nitric acid HNO_3 can finally be produced through the gradual oxidation of NO_x mediated by ·H, ·OH, and HO_2· radicals that formed from the dissociation of water molecules [58, 59].

In general, DBDs can operate in two different modes with respect to the prevailing gaseous product: O_3 vs. NO_x mode [82]. While the O_3 mode is characterized by low discharge powers (energy densities) with a dominant production of O_3, the NO_x mode prevails for high discharge powers with significant production of NO and NO_2. Unlike O_3 which is usually considered as a desired product for its strong oxidizing properties applicable in many applications, a situation regarding NO_x is more complicated. The NO_x production can have an adverse effect during the gas cleaning process as the NO_x usually reacts with reaction intermediates and produces even more toxic substances [83]. On the other hand, when the discharge is generated in contact with a liquid, the NO_x can be dissolved in it, thus producing nitrites NO_2^- and nitrate NO_3^- desirable for biomedical/agro applications [84, 85]. For this reason, it is highly expected that the presence of water (or humidity in the gas phase) may have a significant effect on the composition and concentrations of gaseous products of

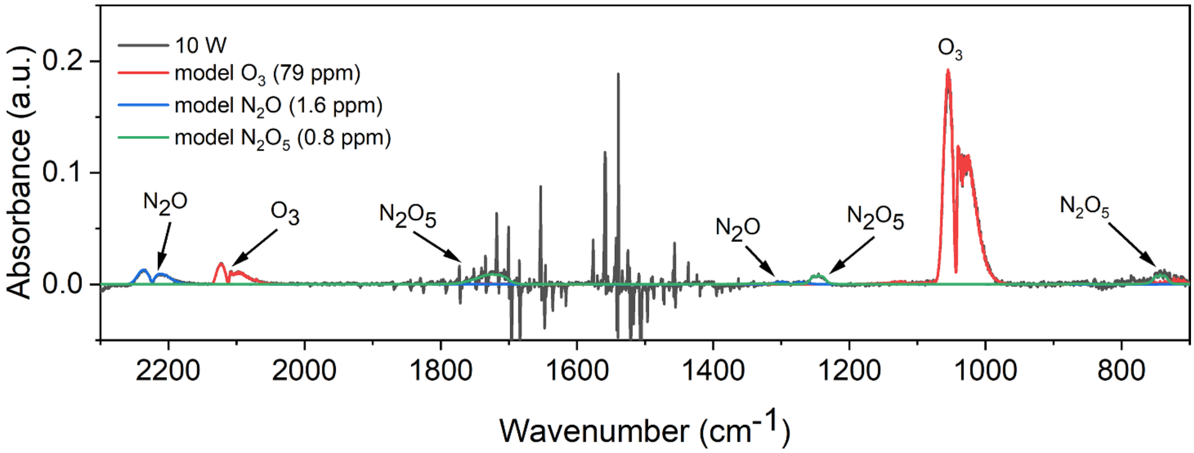

Figure 5. Infrared absorption spectrum of gaseous products of the discharge at discharge power of 10 W. The modeled spectra of O_3, N_2O, and N_2O_5 corresponding to respective species concentrations are also presented.

the discharge. Additionally, increased humidity can significantly alter the discharge properties which, in turn, affect the discharge electrical characteristics and production of reactive species, too [86]. Therefore, before using the discharge in contact with any liquid (e.g. water) in any application, trends of production of gaseous species by the discharge should be characterized under various operating conditions.

Figure 5 depicts the infrared absorption spectrum of gaseous species produced by the discharge. As can be seen, only O_3, N_2O, and N_2O_5 were detected under the investigated operating conditions. These modeled spectra were aligned with respective species concentrations and added to figure 5. Other species (NO, NO_2, HNO_2, HNO_3), that were also expected to be present, were not found in the FTIR spectra. The absence of NO and NO_2 in the spectra indicates either their low concentrations below the detection limit of the setup (approx. 7 ppm for NO and 1.5 ppm for NO_2) or their fast oxidation into N_2O_5 mediated by O_3 [87]. The second explanation can be supported by the fact that O_3 was found as the dominant gaseous product under all investigated conditions. The presence of water vapors can lead to the production of HNO_2 and HNO_3 which are other expected gaseous products. However, their absence in the FTIR spectra may also indicate either their concentrations below the detection limit of the setup (approx. 1.5 ppm) or their rapid dissolution in the present water due to very high Henry's law solubility coefficients [58]. Based on the results we may conclude the discharge was operated only in O_3 mode without significant formation of NO, NO_2, HNO_2, and HNO_3 in the gas phase under all operating conditions tested in this study.

Figure 6 shows the O_3 concentration as a function of the treatment time at various discharge powers. After discharge ignition, the O_3 concentration initially increased due to the prevailing rate of O_3 formation over its decomposition. After some time of discharge operation (approx. 5 min), the processes of O_3 formation and decomposition balanced, so the O_3 concentration culminated and stabilized. The temporal evolution of N_2O and N_2O_5 concentrations followed the same pattern.

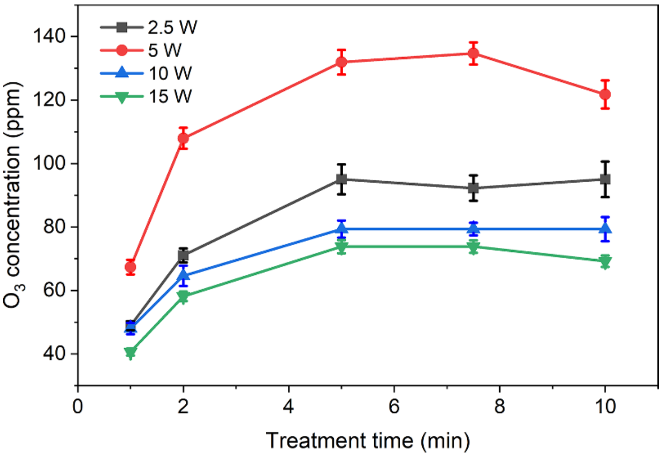

Figure 6. Temporal evolution of O_3 concentration as a function of discharge power.

With an increase in discharge power from 2.5 to 5 W, the O_3 concentration increased and reached maximum values. However, with a further increase of power from 5 to 15 W, the O_3 concentration significantly decreased (figure 6). This trend can be explained by the processes of O_3 decomposition becoming more dominant with increasing the discharge power. More specifically, the increase of discharge power results in a more intense discharge which in turn increases the temperature of water as well as the gas surrounding the discharge which reduces the O_3 formation. This further leads to an increase in gas humidity due to a higher rate of evaporation from the water surface, also resulting in O_3 reduction.

At higher temperatures, the recombination reactions of O_3 with O_2 molecules as well as excited oxygen atoms $O(^1D)$ become dominant [88, 89] as a result of the exponential dependence of their reaction rates on temperature [90, 91]. In addition to direct recombination reactions of O_3, the consumption of ·O atoms should be also considered as they are essential precursors of O_3 production. At higher gas temperatures, ·O atoms can be effectively consumed by

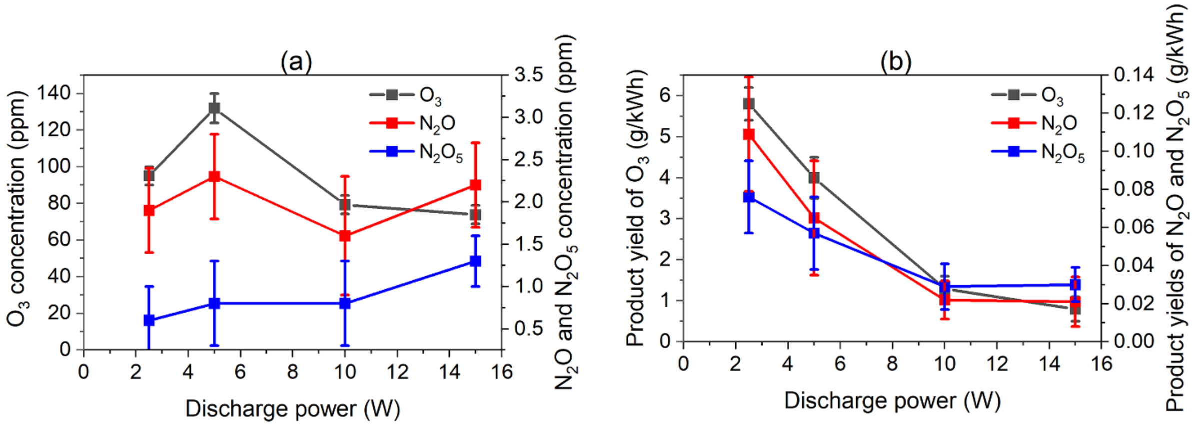

Figure 7. Concentrations (a), and production yields (b) of O_3, N_2O, and N_2O_5 as functions of discharge power.

reactions with N_2 molecules leading to lower O_3 production [83, 92]. Furthermore, consumption of ·O atoms accelerates with an increase of the gas humidity due to reactions with ·OH and HO_2· radicals formed from the dissociation of H_2O or direct reactions with H_2O molecules themselves [93]. Another possible pathway for O_3 decomposition is its direct reaction with ·H, ·OH, and HO_2· radicals [94–96]. Hence, both higher temperature and higher relative humidity of the gas have an adverse effect on O_3 concentration and may explain its observed decrease at higher discharge powers (>5 W).

Figures 7(a) and (b) present the O_3, N_2O, and N_2O_5 stabilized concentrations obtained during the discharge operation and their corresponding production yields, respectively. As discussed earlier, the maximum O_3 concentration (approx. 132 ppm) was obtained at 5 W, and with further increase of the discharge power, its concentration decreased (figure 7(a)). On the other hand, for both N_2O and N_2O_5, the situation was different. The production of N_2O by the discharge can be affected by many aspects. An increasing discharge power and more intense discharge may lead to a higher yield of the $N_2(A)$ excited species essential for N_2O production. On the other hand, higher discharge power results in a higher rate of evaporation from the water surface and, thus, a higher gas humidity level that generally decreases the generation rates of the $N_2(A)$ and other N-containing species. This can be associated with a decrease in dissociation and excitation reaction rates when electrons collide with N_2 molecules [86]. Besides, H_2O molecules provide a very efficient quenching of $N_2(A)$ species [97]. In our study, the N_2O concentration showed fluctuations with increased discharge power, reaching maximum values of approx. 2.3 ppm. We suppose the resulting ambiguous trend is given by a balance among various conflicting effects affecting the N_2O formation. On the contrary, the N_2O_5 concentration slightly increased within the whole range of discharge powers and reached approx. 1.3 ppm at 15 W (figure 7(b)).

The PYs of O_3, N_2O, and N_2O_5 collectively exhibited a monotonic decrease with increasing discharge power up to 10 W. With a further increase to 15 W, the PYs of all compounds showed no significant variations (figure 7(b)). The maximal PY of N_2O and N_2O_5 were low (0.11 and 0.08 g kWh^{-1}, respectively), whereas the maximal PY of O_3 was higher (5.8 g kWh^{-1}), but still substantially smaller than the common values obtained with various air discharges reported by other authors (typically in a range of 40–100 g kWh^{-1}) [87, 98, 99]. However, most of their discharges that reached high PY of O_3 were operated in dry gases (i.e. no humidity or liquid water present). This implies that the presence of water in the reactor and associated humidity in the gas significantly reduces the energy efficiency of O_3 production. In addition to the general negative effect of the gaseous humidity on the O_3 production described earlier, this can also be explained by distinctive energy losses and Joule heating of the water present when the discharge is in direct contact with it [96]. However, the achieved PY of O_3 results are comparable to other discharges that have been generated in contact with liquids (e.g. Lukeš *et al* obtained PY of O_3 ~5 g kWh^{-1} with a pulsed corona discharge under comparable operating conditions) [96].

3.2.1. In-situ O_3 detection by UV–VIS absorption technique.

Figure 8 illustrates the results of *in-situ* O_3 mapping in the open reactor using UV–VIS absorption spectroscopy. The O_3 concentration is highest near the discharge, particularly close to the liquid surface. The O_3 concentration gradually decreases as the measurement UV–VIS light beam moves upward along the discharge area. This decrease is likely due to the reduced intensity of plasma filaments and the electric field, as well as the dilution of ozone in the surrounding air.

Nevertheless, ozone concentrations are the highest near the three-phase boundary point boundary, indicating that oxidative species are primarily localized within the plasma region. This localization favors the oxidation and functionalization of the polymer surfaces.

3.3. Liquid analysis

3.3.1. Measurements of PAW parameters.

Operation of SDBD using the liquid electrodes with tap water leads to an increase in the temperature of generated PAW, as shown in

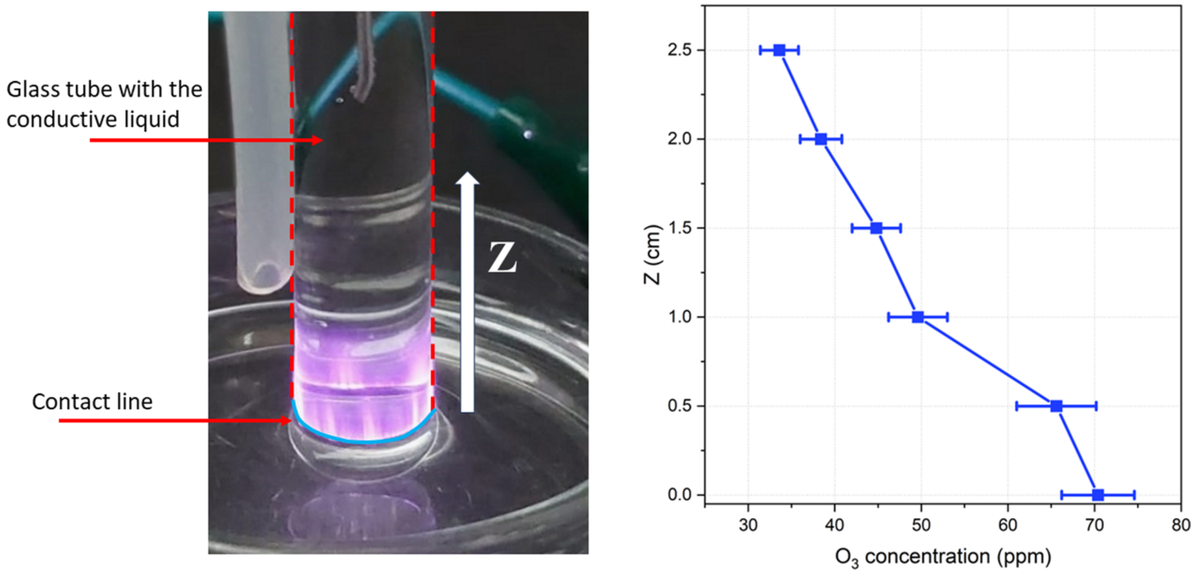

Figure 8. Mapping of the ozone concentration alongside the glass tube at a discharge power of 15 W by *in-situ* UV–VIS absorption spectroscopy.

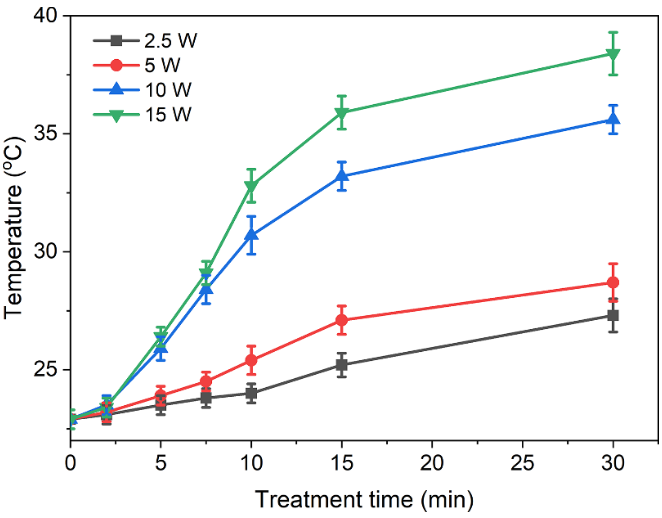

Figure 9. Temporal evolution of water temperature as a function of discharge power.

figure 9. Initially, the temperature increase is notably more pronounced within the first 15 min. For instance, when operated at 15 W, the temperature escalates from ambient conditions (23 °C) to 36 °C, and in the subsequent 15 min, it increases by only approximately 2 °C. This trend of temperature increment is consistently observed at reduced discharge powers of 2.5 W, 5 W, and 10 W. The diminishing rate of temperature increase seems to reach a maximum plateau after 15 min, implying progress toward the thermal equilibrium of the system. Consequently, the maximum water temperature generated by plasma in this configuration after 30 min of activation at discharge powers of 2.5, 5, 10, and 15 W was 27.3 °C, 28.7 °C, 35.6 °C, and 38.4 °C, respectively. This pattern of temperature rise over time was also illustrated in DBD-treated PAW [100].

The pH of SDBD-treated tap water was approximately 7.8 ± 0.3, throughout the 30 min treatment duration, which did not significantly change from its initial value of 7.9. This observation of stable pH levels or minimal pH changes in tap water post-treatment aligns with the findings reported in [100] and [101] and can be explained by its weak bicarbonate buffering capacity. On the other hand, when de-ionized or distilled water is used as the treated solution, the pH tends to decline more rapidly [102, 103]. Furthermore, a difference in pH behavior was reported in scenarios where water is either stirred or remains static during plasma treatment [104]. In the static condition, the pH does not alter significantly, attributed to the slow diffusion of RONS, compared to the scenario where water is stirred. Additionally, a study noted a pH decrease below 3 after 20 min of DBD treatment in 1 l of circulating tap water which enhanced the diffusion of reactive species in the water, thereby reducing the pH of PAW [105].

Electrical conductivity serves as a valuable indicator of ion concentration within the water. In this study, the conductivity increased from 420 μS cm^{-1} (tap water) to 520 μS cm^{-1} over a 30 min treatment period. This indicates that the discharge current passing through the liquid remained stable throughout the 30 min treatment duration.

3.3.2. *Visualization of ROS propagation.*

To visualize the penetration of RONS into the liquid, a photo sequence presented in figure 10 was taken. A rectangular glass cuvette containing 20 ml of KI-starch solution was utilized to enhance the visualization of ROS generation and propagation. During the experiment, the solution was not stirred.

Under the influence of an electric field, a distinct Taylor cone emerges, prominently captured in the photos. ROS generation predominantly occurs within the plasma region, closely adjacent to the glass tube, indicating chemical reactions at the gas/liquid interface. Subsequently, ROS propagates primarily

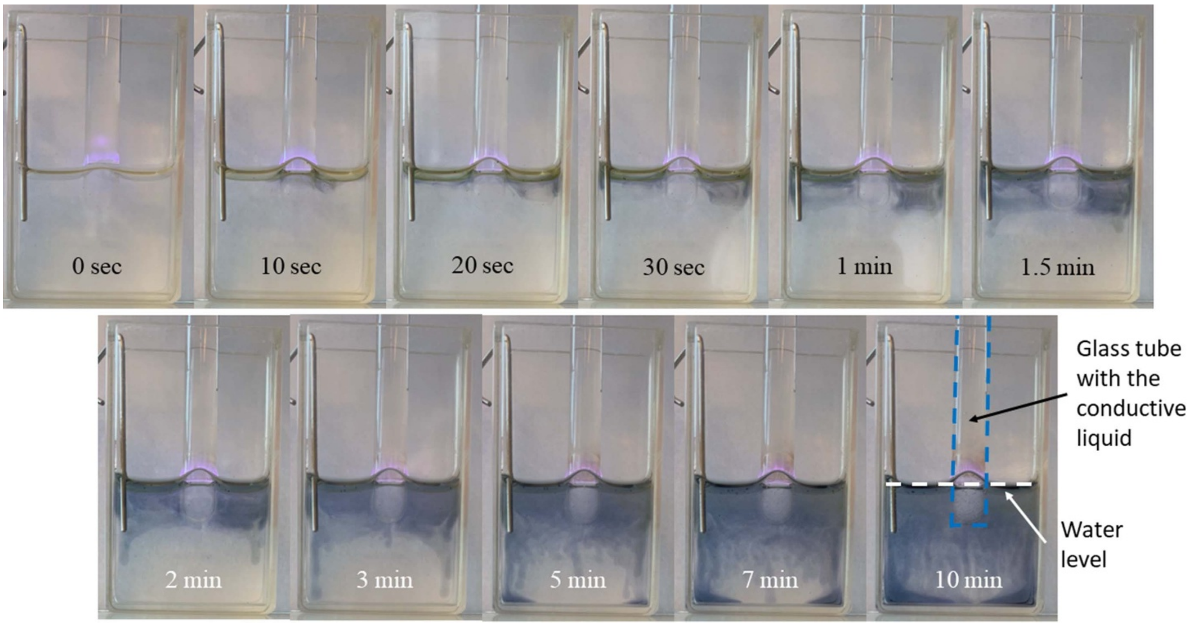

Figure 10. A photo sequence of the ROS generation and propagation during the 15 W discharge power.

along the liquid surface, with minimal penetration into the bulk solution. Upon contacting the cuvette walls, ROS further spreads along them and gradually sinks to the bottom. Within a span of 10 min, the whole liquid volume turns blue, which proves that even without stirring, comparatively high concentrations of ROS are present in the whole liquid volume. These observations corroborate previous findings indicating that akin to the aforementioned ROS, other RONS exhibit similar behavior during liquid treatment in various studied systems [106, 107].

3.3.3. Determination of RONS in PAW. As outlined in the previous section, ozone was identified in substantial quantities in the gas phase compared to other species. Despite its high concentration generation in the gas phase, its presence in the liquid was measured in the micromolar range only. Hassan *et al* [108] have documented that the transport of ozone into the liquid is constrained by its low Henry's law solubility coefficient and is significantly influenced by the area of the plasma–liquid interface. Ozone is initially produced in the gas phase and subsequently transferred into the liquid, as illustrated in reaction (2),

$$\mathrm{O}\cdot + \mathrm{O}_2 + \mathrm{M} \rightarrow \mathrm{O}_3 + \mathrm{M} \rightarrow \mathrm{O}_{3(\mathrm{aq})}. \qquad (2)$$

Figure 11 illustrates the dynamics of ozone concentration in PAW over a 30 min treatment duration and across various discharge powers. At the discharge power of 5 W, the gas phase contained approximately 132 ppm of ozone, yet the corresponding concentration in the liquid phase after 30 min was only 4.52 ppm (94 μM), underscoring ozone's limited solubility in water as previously highlighted [108]. In our analysis, however, a notable increase in ozone concentration was observed in the water with the increase in discharge power, not correlating with its gaseous concentration (figure 6).

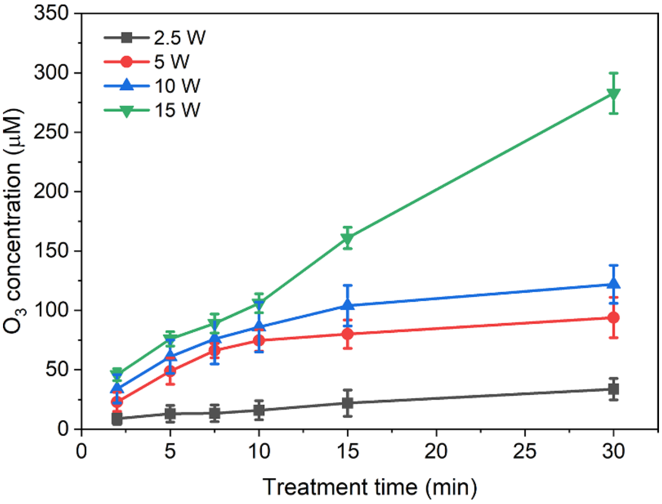

Figure 11. Temporal evolution of O_3 concentration as a function of discharge power.

Tarabova *et al* [63] discussed the specificity of the indigo blue assay for O_3 detection in PAW and specified that OH radical can decolorize the indigo dye perturbing the detection of O_3 in PAW. Therefore, the concentration of ozone represented here can be overestimated, especially for higher discharge powers and treatment time.

In our study, plasma is generated directly in contact with the water surface, enabling short-lived species such as hydroxyl (OH) radicals to be swiftly dissolved into the water, thereby facilitating various chemical pathways. Near the interface between the plasma, water, and the polymer test tube, the temperature rises sufficiently to facilitate the water evaporation. The presence of water vapor in air can contribute to the formation of OH radicals through the electron-impact dissociation of water molecules, as described by reaction (3) [109]. This fact can explain a continuous increase of ozone concentration in water for 15 W discharge power even though its concentration reduces in the gas phase. Additionally, in air discharges, OH radicals can also be produced via reaction (4), involving atomic oxygen [110]. There is also a potential for atomic oxygen to react with hydrogen peroxide H_2O_2, yielding HO_2 and OH radicals through reaction (5). Moreover, plasma-induced UV photolysis is capable of directly generating OH radicals in the water via reaction (6) [111, 112]. Other possible mechanisms include electron–ion dissociative recombination (reactions (7) and (8)) and the recombination of positive and negative ions (reactions (9) and (10)),

$$\mathrm{e} + \mathrm{H_2O} \rightarrow \mathrm{e} + \cdot\mathrm{OH} + \mathrm{H} \tag{3}$$

$$\mathrm{O}\left({}^1\mathrm{D}\right) + \mathrm{H_2O} \rightarrow \cdot\mathrm{OH} + \cdot\mathrm{OH} \tag{4}$$

$$\mathrm{H_2O_2} + \mathrm{O}\left({}^1\mathrm{D}\right) \rightarrow \cdot\mathrm{HO_2} + \cdot\mathrm{OH} \tag{5}$$

$$\mathrm{H_2O_{(aq)}} \overset{\mathrm{UV}}{\rightarrow} \cdot\mathrm{H_{(aq)}} + \cdot\mathrm{OH_{(aq)}} \tag{6}$$

$$\mathrm{e}^- + \mathrm{H_2O^+} \rightarrow \cdot\mathrm{OH} + \cdot\mathrm{H} \tag{7}$$

$$\mathrm{e}^- + \mathrm{H_3O^+} \rightarrow \cdot\mathrm{OH} + \mathrm{H_2} + \mathrm{e} \tag{8}$$

$$\mathrm{H}^- + \mathrm{H_2O^+} \rightarrow \cdot\mathrm{OH} + \mathrm{H_2} \tag{9}$$

$$\mathrm{H}^- + \mathrm{H_3O^+} \rightarrow \cdot\mathrm{OH} + \mathrm{H_2} + \cdot\mathrm{H}\,. \tag{10}$$

Hydrogen peroxide (H_2O_2) stands out as a crucial long-lived ROS in PAW, recognized for its pivotal role across various applications, particularly in the medical field. Numerous studies have highlighted its significance as a fundamental molecule offering antimicrobial capabilities and promoting wound healing, underpinning its utility in plasma-based medical treatments [113–115]. Beyond its medical applications, hydrogen peroxide has been acknowledged for its positive impact on plant growth, its ability to diminish pathogen virulence, and its effectiveness in reducing the expression of disease symptoms [116, 117].

The generation of H_2O_2 in PAW is attributed to both the dissolution of gas-phase H_2O_2 and its formation within the liquid through various pathways. OH radicals, identified as crucial precursors for H_2O_2 formation, undergo numerous reactions contributing to its formation. OH radicals lead to the formation of H_2O_2 in the gas phase through two-body recombination, represented by reaction (11). This gas-phase H_2O_2 subsequently dissolves in water to form aqueous $H_2O_{2(aq)}$, facilitated by its very high Henry's law solubility constant ($k_H \approx 9 \times 10^2$ mol m^{-3} Pa^{-1}) [108]. In addition to this mechanism, several other pathways are crucial for H_2O_2 production in PAW. The OH radical, once dissolved in PAW, can directly lead to H_2O_2 formation within the liquid by reaction (12) [118]. Beyond the role of OH radicals, peroxyl (HO_2) radicals are also capable of generating H_2O_2 in the liquid phase through reactions (13)–(16). Furthermore, the attachment of electrons to O_2 molecules initiates a series of reactions (17)–(20) resulting in the liquid-phase formation of H_2O_2, as documented in [119],

$$\cdot\mathrm{OH} + \cdot\mathrm{OH} \rightarrow \mathrm{H_2O_2} \rightarrow \mathrm{H_2O_{2(aq)}} \tag{11}$$

$$\cdot\mathrm{OH_{(aq)}} + \cdot\mathrm{OH_{(aq)}} \rightarrow \mathrm{H_2O_{2(aq)}} \tag{12}$$

$$\cdot\mathrm{H} + \mathrm{O_2} \rightarrow \cdot\mathrm{HO_2} \tag{13}$$

$$\cdot\mathrm{OH} + \mathrm{O_3} \rightarrow \mathrm{HO_2} + \mathrm{O_2} \tag{14}$$

$$\cdot\mathrm{H} + \cdot\mathrm{HO_2} \rightarrow \mathrm{H_2O_2} \tag{15}$$

$$\mathrm{HO_{2(aq)}} + \mathrm{HO_{2(aq)}} \rightarrow \mathrm{H_2O_{2(aq)}} + \mathrm{O_{2(aq)}} \tag{16}$$

$$\mathrm{O_2} + \mathrm{e} \rightarrow \mathrm{O_2^-} \tag{17}$$

$$\mathrm{O_2^-} + \mathrm{H^+} \rightarrow \mathrm{HO_2} \tag{18}$$

$$\mathrm{HO_{2(aq)}} + \mathrm{e_{(aq)}} \rightarrow \mathrm{HO^-_{2(aq)}} \tag{19}$$

$$\mathrm{HO^-_{2(aq)}} + \cdot\mathrm{H} \rightarrow \mathrm{H_2O_{2(aq)}}\,. \tag{20}$$

Figure 12 illustrates the relationship between the measured concentration of aqueous H_2O_2, treatment duration, and discharge power. Several research groups indicated that the treatment time and the discharge power are the key factors that lead to a linear increase in the concentration of H_2O_2 generated within plasma–water systems [20, 120, 121]. As discussed in the previous section, a rise in the discharge power not only intensifies the discharge but also expands its area, potentially enhancing the production of RONS in the gas phase and their transfer to the water, as evidenced in figures 12–14.

In acidic conditions (pH $<$ 3.3), the reaction between H_2O_2 and NO_2^- leads to the formation of peroxynitrite (reactions (21) and (22)), which subsequently decomposes into nitrate (NO_3^-) [9, 63]. However, in our scenario involving SDBD-treated tap water, the pH of the PAW remains stable at approximately 7.8, thus restricting peroxynitrite formation. This pH stability enabled an increase in the concentrations of both H_2O_2 and NO_2^- over the treatment duration, as shown in figures 12 and 13,

$$\mathrm{NO^-_{2(aq)}} + \mathrm{H_2O_{2(aq)}} + \mathrm{H^+} \rightarrow \mathrm{O{=}NOOH_{(aq)}} + \mathrm{H_2O} \tag{21}$$

$$\mathrm{O{=}NOOH_{(aq)}} \leftrightarrow \mathrm{NO^-_{3(aq)}} + \mathrm{H^+}. \tag{22}$$

Nitrites and nitrates play significant roles in PAW due to their antibacterial properties and their ability to act

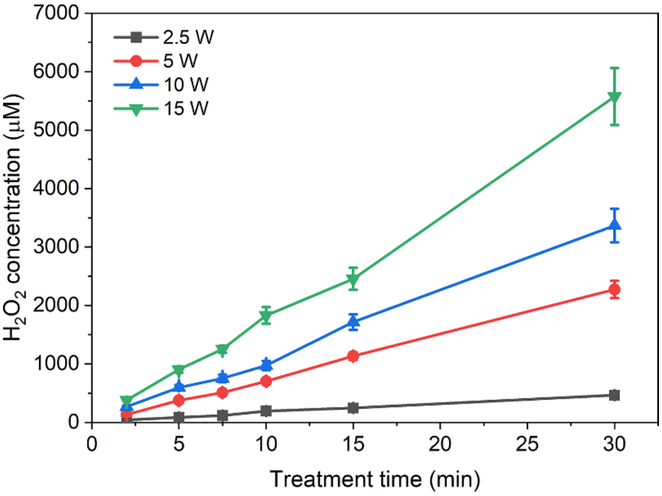

Figure 12. Temporal evolution of aqueous H_2O_2 concentration in PAW as a function of discharge power.

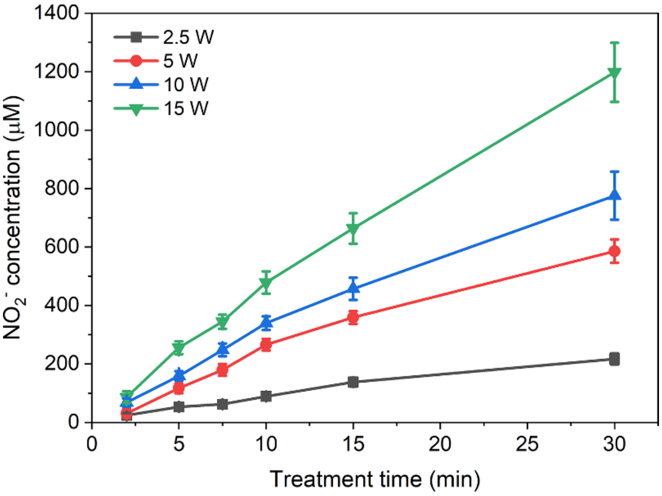

Figure 13. Temporal evolution of aqueous NO_2^- concentration in PAW as a function of discharge power.

e.g. as organic fertilizers, enhancing plant growth [122, 123]. These species are primarily generated in PAW through the dissolution of gas-phase NO_x compounds, including NO, NO_2, HNO_2, and HNO_3 [59]. Janda *et al* [59] highlighted that humidity facilitates the conversion of gas-phase NO_2 into HNO_2, which then much better dissolves in PAW to yield nitrite ions. Since NO has a low Henry's solubility constant ($k_H \approx 1.9 \times 10^{-5}$ mol m^{-3} Pa^{-1}), it contributes minimally to the aqueous NO_x- concentrations. In our FTIR analysis, none of these reactive species were detected in the gas phase, suggesting the possibility that HNO_2 ($k_H \approx 4.8 \times 10^{-1}$ mol m^{-3} Pa^{-1}) and HNO_3 ($k_H \approx 2.1 \times 10^3$ mol m^{-3} Pa^{-1}), formed in the gas phase through reactions (23) and (24), and thanks to having high solubility coefficients, they quickly dissolved in water without being detected by FTIR after gas samples were sucked from the discharge volume. These compounds significantly contribute to the aqueous concentrations of NO_2^- and NO_3^- through reactions (25) and (26). NO_3^- could also result from the reaction between NO_2^- and O_3 (reaction (27)), with dissolved NO and NO_2 from the gas further contributing to the formation of NO_3^- and NO_2^- in PAW through reactions (28) and (29),

$$\cdot OH + NO + M \rightarrow HNO_2 + M \tag{23}$$

$$\cdot OH + NO_2 + M \rightarrow HNO_3 + M \tag{24}$$

$$HNO_{3(aq)} \leftrightarrow NO^-_{3(aq)} + H^+ \tag{25}$$

$$HNO_{2(aq)} \leftrightarrow NO^-_{2(aq)} + H^+ \tag{26}$$

$$NO^-_{2(aq)} + O_{3(aq)} \rightarrow NO^-_{3(aq)} + O_{2(aq)} \tag{27}$$

$$NO_{2(aq)} + NO_{2(aq)} + H_2O \rightarrow NO^-_{2(aq)} + NO^-_{3(aq)} + 2H^+ \tag{28}$$

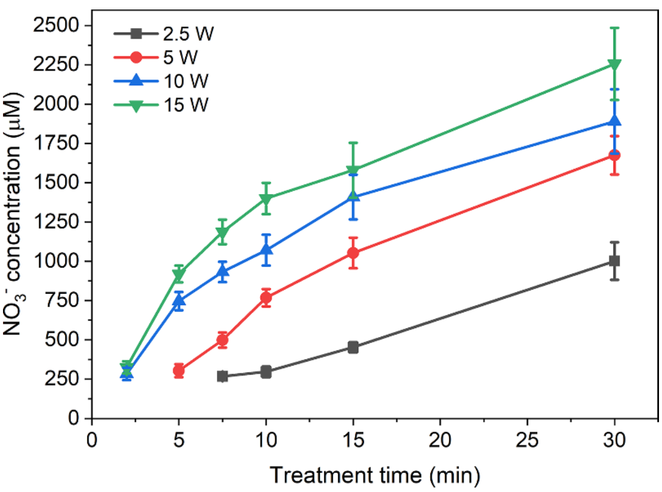

Figure 14. Temporal evolution of the aqueous NO_3^- concentration in PAW as a function of discharge power.

$$NO_{(aq)} + NO_{2(aq)} + H_2O \rightarrow 2NO^-_{2(aq)} + 2H^+. \tag{29}$$

Figures 13 and 14 illustrate the varying concentrations of nitrates and nitrites in PAW as a function of treatment duration and the applied discharge power. Similar to the behavior observed for H_2O_2, the concentrations of both NO_2^- and NO_3^- increased with the increasing discharge power. This trend could be associated with enhanced production of NO_x species in the gas phase as the discharge power rose and hence more production in the liquid. As the treatment time increases, more reactive species accumulate in the PAW due to continuous production in the gas and dissolution in the liquid. This accumulation and its effects are further understood by the visualization of ROS deposition through SDBD in figure 9.

It is essential to simplify the operation of plasma–liquid systems and the production of PAW for its future everyday practical use. Our study introduces a simple and innovative

Table 1. Comparison of RONS in PAW with SDBD's reported in literature, DI-de-ionized water, DW-distilled water, TW-tap water, PBS-phosphate buffer saline.

Configuration	(Solution, treatment time, volume, initial pH)	Power/voltage	pH	(H_2O_2, NO_2^-, NO_3^-, O_3)
Our SDBD	(TW, 10 min, 10 ml, 7.8)	15 W	7.8	(1.829 mM, 0.478 mM, 1.4 mM, 0.106 mM)
In-plane DBD [125]	(DW, 10 min, 3 ml, 7)	200 W	3.5	(1 mM, 5 mM, 1 mM, 10 μM)
Volumetric DBD [124]	(DI,10 min, 20 ml, 5)	6.7 W	4.5	(0.293 mM, -,-, 4.166 mM)
SDBD [44]	(DI, 30 min, 100 ml)	65 W	1.93	(1.52 mM,-,-,-)
SDBD [126]	(NaCl, 6 min, 5 ml,6.5)	17 kV	2.51	(59 μM, 86.2 μM, 2.0512 mM, -)
SDBD [43]	(DW, 30 min, 5 ml,7.5)	14 W	2.66	(21.1 μM, 0.1402 mM, 3.4029 mM,-)
DBD [39]	(PBS, 5 min,0.15 ml,7.4)	5.22 W 0.87 W	6.6 7	(0.07 mM, 1.8 mM, 0.5 Mm, -) (0, 0, 0, 62.5 μM)

setup for generating PAW rich in RONS. Despite the relatively small plasma area in our SDBD setup, we detected significant levels of RONS (O_3, H_2O_2, NO_2^-, and NO_3^-) in PAW, influenced by the treatment time and input power. Hänsch *et al* [43] modified the dielectric layer of SDBD to ceramic for enhanced durability and corrosion resistance, affecting the composition of RONS in PAW. In our design, we utilized a basic glass tube as the dielectric layer, ensuring prolonged use with minimal byproducts in PAW and an easy replacement of the dielectric material. Scaling up PAW production is feasible by deploying multiple such tubes simultaneously. Table 1 lists several studies that predominantly used SDBD above the water surface or volume DBD with a water electrode. In these studies (except [124]), reactive species were generated in the gas phase and then dissolved in the liquid phase, contributing to RONS formation in the liquid. Our results indicate that direct interaction between plasma and liquid leads to higher concentrations of H_2O_2 produced by our SDBD reactor compared to concentrations reported in the literature (table 1) for indirect treatment methods. This highlights the significance of direct plasma–liquid interaction for PAW generation, as it allows gaseous H_2O_2 as well as short-lived species like OH and HO_2 to contribute to the formation of aqueous H_2O_2 in PAW.

Pavlovich *et al* [39] and Hänsch *et al* [43] have reported the presence of O_3, NO_2, N_2O, N_2O_5, and HNO_3 in the gas phase using FTIR measurements with SDBD, contributing to the formation of liquid-phase species. However, in our study, FTIR measurements only detected N_2O, O_3, and N_2O_5 in the gas phase. Despite this, we observed sufficient concentrations of NO_3^-, NO_2^-, and H_2O_2 in the liquid phase. This suggests that highly soluble species like HNO_2, HNO_3, and NO_2 may have already dissolved in the liquid before being sampled for FTIR analysis, contributing to the presence of liquid NO_2^- and NO_3^-. Aqueous $O_{3(aq)}$ formation depends solely on the dissolution of ozone from the gas phase. Neretti *et al* [124] reported the significance of gas temperature in ozone production in water by examining nanosecond pulse discharge and sinusoidal discharge in volumetric DBD with water serving as one of the electrodes. They found that nanosecond pulse discharge, characterized by lower gas temperatures (318 K), resulted in higher concentrations of ozone in the liquid compared to sinusoidal discharge (425 K). Pavlovich *et al* [39] noted that both gas and liquid phases exhibited an increase in NO_x components with increasing power, while O_3 was only detected at low powers (table 1). Moreover, the strong correlation between aqueous ozone concentration and the inactivation of *Escherichia coli* underscored the ozone's pivotal role in bacterial inactivation [39]. In our case, employing liquid electrodes in SDBD, ozone was detected in substantial amounts depending upon the treatment time. This mixture of RONS in PAW can be thus utilized for various bio-medical and agricultural applications.

Given the intricate interplay of various parameters influencing the composition of RONS in PAW, accurate comparison of different geometries presents a challenge. Nonetheless, it is evident that liquid electrode SDBD yields comparable, if not greater, RONS composition in PAW. Such a 3-phase interface setup offers several application possibilities simultaneously: continuous functionalization of the material used as a dielectric, direct and indirect disinfection of dielectric surfaces, alongside with PAW production.

4. Conclusion

The integration of the SDBD at the gas/liquid/solid interface represents a novel approach in water treatment methods, as well as dielectric surface treatments, that has not been previously documented in scientific literature.

In this study, the electrical measurements of such SDBD discharge are presented and its characteristics are discussed. Species such as O_3, N_2O, and N_2O_5 were detected in the gas phase during the discharge operation. Their concentration and time evolution were measured and quantified by using FTIR and *in-situ* UV–VIS absorption analyses. Also, the production yields of these species were calculated.

Furthermore, comprehensive measurements of RONS within the plasma-treated water in such a system have also been notably absent from prior research efforts. This study tries to connect these critical gaps by exploring the potential of SDBD in treating tap water, and by quantifying the presence and impact of RONS within the water. We shed light on the mechanisms of their production and the efficiency of the system. Despite the challenges posed by the presence of water vapor in the plasma, which can attenuate certain plasma reactions in the gas phase, our findings demonstrate comparatively high efficiency of RONS production in water. Notably, the observed buffer capabilities of tap water ensure a consistent presence of NO_2^-. Through visualization experiments, we illustrate the rapid propagation of reactive species throughout the liquid volume, suggesting promising prospects for efficient and thorough water treatment processes.

The scalability of the presented system underscores its practical viability. We believe that the results presented will stimulate basic research of SDBD configuration described in this paper, which can be useful for a wide variety of practical applications not restricted to the mentioned ones.

Data availability statement

All data that support the findings of this study are included within the article (and any supplementary files).

Acknowledgment

This work was funded by the EU NextGenerationEU through the Recovery and Resilience Plan for Slovakia under the Project No. 09I03-03-V04-00094 and by Marie S Curie Action Postdoctoral Fellowship under Horizon Europe with Grant Agreement Number 101066764.

ORCID iDs

Oleksandr Galmiz https://orcid.org/0000-0002-2815-180X
Richard Cimerman https://orcid.org/0000-0001-8854-320X
Pankaj Pareek https://orcid.org/0009-0009-0968-2160
Mário Janda https://orcid.org/0000-0001-9051-4221
Zdenko Machala https://orcid.org/0000-0003-1424-1350

References

[1] Ito M, Oh J S, Ohta T, Shiratani M and Hori M 2018 Current status and future prospects of agricultural applications using atmospheric-pressure plasma technologies *Plasma Process. Polym.* **15** e1700073

[2] Puač N, Škoro N, Spasić K, Živković S, Milutinović M, Malović G and Petrović Z L 2018 Activity of catalase enzyme in Paulownia tomentosa seeds during the process of germination after treatments with low pressure plasma and plasma activated water *Plasma Process. Polym.* **15** 1700082

[3] Sivachandiran L and Khacef A 2017 Enhanced seed germination and plant growth by atmospheric pressure cold air plasma: combined effect of seed and water treatment *RSC Adv.* **7** 1822–32

[4] Graves D B 2014 Reactive species from cold atmospheric plasma: implications for cancer therapy *Plasma Process. Polym.* **11** 1120–7

[5] Bekeschus S, Schmidt A, Weltmann K D and von Woedtke T 2016 The plasma jet kINPen—a powerful tool for wound healing *Clin. Plasma Med.* **4** 19–28

[6] Schmidt A, Bekeschus S, Wende K, Vollmar B and von Woedtke T 2017 A cold plasma jet accelerates wound healing in a murine model of full-thickness skin wounds *Exp Dermatol.* **26** 156–62

[7] Thirumdas R, Sarangapani C and Annapure U S 2015 Cold plasma: a novel non-thermal technology for food processing *Food Biophys.* **10** 1–11

[8] Misra N N, Schlüter O and Cullen P J 2016 *Cold Plasma in Food and Agriculture: Fundamentals and Applications* (Elsevier Inc.)

[9] Lukes P, Dolezalova E, Sisrova I and Clupek M 2014 Aqueous-phase chemistry and bactericidal effects from an air discharge plasma in contact with water: evidence for the formation of peroxynitrite through a pseudo-second -order post-discharge reaction of H_2O_2 and HNO_2 *Plasma Sources Sci. Technol.* **23** 015019

[10] Woedtke T, Von, Oehmigen K, Brandenburg R, Hoder T, Wilke C, Hähnel M and Weltmann K Plasma-liquid-interactions : chemistry and antimicrobial effects pp 39–40

[11] Traylor M J, Pavlovich M J, Karim S, Hait P, Sakiyama Y, Clark D S and Graves D B 2011 Long-term antibacterial efficacy of air plasma-activated water *J. Phys. D: Appl. Phys.* **44** 472001

[12] Hongzhuan Z *et al* 2020 Preparation of the inactivated Newcastle disease vaccine by plasma activated water and evaluation of its protection efficacy *Appl. Microbiol. Biotechnol.* **104** 107–17

[13] Ten Bosch L, Köhler R, Ortmann R, Wieneke S and Viöl W 2017 Insecticidal effects of plasma treated water *Int. J. Environ. Res. Public Health* **14** 1460

[14] Rathore V, Patel D, Shah N, Butani S, Pansuriya H and Nema S K 2021 Inactivation of Candida albicans and lemon (Citrus limon) spoilage fungi using plasma activated water *Plasma Chem. Plasma Process.* **41** 1397–414

[15] Machala Z, Chldekov L and Pelach M 2010 Plasma agents in bio-decontamination by dc discharges in atmospheric air *J. Phys. D: Appl. Phys.* **43** 222001

[16] Machala Z, Tarabova B, Hensel K, Spetlikova E, Sikurova L and Lukes P 2013 Formation of ROS and RNS in water electro-sprayed through transient spark discharge in air and their bactericidal effects *Plasma Process. Polym.* **10** 649–59

[17] Rathore V and Nema S K 2022 A comparative study of dielectric barrier discharge plasma device and plasma jet to generate plasma activated water and post-discharge trapping of reactive species *Phys. Plasmas* **29** 033510

[18] Lu X, Naidis G V, Laroussi M, Reuter S, Graves D B and Ostrikov K 2016 Reactive species in non-equilibrium atmospheric-pressure plasmas: generation, transport, and biological effects *Phys. Rep.* **630** 1–84

[19] Bruggeman P J *et al* 2016 Plasma–liquid interactions: a review and roadmap *Plasma Sources Sci. Technol.* **25** 053002

[20] Chauvin J, Judée F, Yousfi M, Vicendo P and Merbahi N 2017 Analysis of reactive oxygen and nitrogen species generated in three liquid media by low temperature helium plasma jet *Sci. Rep.* **7** 1–15

[21] Hansen L, Schmidt-Bleker A, Bansemer R, Kersten H, Weltmann K D and Reuter S 2018 Influence of a liquid surface on the NO_x production of a cold atmospheric pressure plasma jet *J. Phys. D: Appl. Phys.* **51** 474002

[22] Van Gaens W, Bruggeman P J and Bogaerts A 2014 Numerical analysis of the NO and O generation mechanism in a needle-type plasma jet *New J. Phys.* **16** 063054

[23] Douat C, Hübner S, Engeln R and Benedikt J 2016 Production of nitric/nitrous oxide by an atmospheric pressure plasma jet *Plasma Sources Sci. Technol.* **25** 025027

[24] Uchida G, Nakajima A, Ito T, Takenaka K, Kawasaki T, Koga K, Shiratani M and Setsuhara Y 2016 Effects of nonthermal plasma jet irradiation on the selective production of H_2O_2 and NO_2^- in liquid water *J. Appl. Phys.* **120** 203302

[25] Ogawa K, Oh J S, Gaur N, Hong S H, Kurita H, Mizuno A, Hatta A, Short R D, Ito M and Szili E J 2019 Modulating the concentrations of reactive oxygen and nitrogen species and oxygen in water with helium and argon gas and plasma jets *Jpn. J. Appl. Phys.* **58** SAAB01

[26] Reuter S, Tresp H, Wende K, Hammer M U, Winter J, Masur K, Schmidt-Bleker A and Weltmann K D 2012 From RONS to ROS: tailoring plasma jet treatment of skin cells *IEEE Trans. Plasma Sci.* **40** 2986–93

[27] Janda M, Hensel K and Machala Z 2018 Kinetic plasma chemistry model of pulsed transient spark discharge in air coupled with nanosecond time-resolved imaging and spectroscopy *J. Phys. D: Appl. Phys.* **51** 334002

[28] Janda M, Martišovitš V, Hensel K and Machala Z 2016 Generation of antimicrobial NO_x by atmospheric air transient spark discharge *Plasma Chem. Plasma Process.* **36** 767–81

[29] Park D P, Davis K, Gilani S, Alonzo C A, Dobrynin D, Friedman G, Fridman A, Rabinovich A and Fridman G 2013 Reactive nitrogen species produced in water by non-equilibrium plasma increase plant growth rate and nutritional yield *Curr. Appl. Phys.* **13** S19–S29

[30] Dai X J *et al* 2016 Efficient and selectable production of reactive species using a nanosecond pulsed discharge in gas bubbles in liquid *Plasma Process. Polym.* **13** 306–10

[31] Bian W, Zhou M and Lei L 2007 Formations of active species and by-products in water by pulsed high-voltage discharge *Plasma Chem. Plasma Process.* **27** 337–48

[32] Marouf-Khelifa K, Abdelmalek F, Khelifa A, Belhadj M, Addou A and Brisset J L 2006 Reduction of nitrite by sulfamic acid and sodium azide from aqueous solutions treated by gliding arc discharge *Sep. Purif. Technol.* **50** 373–9

[33] Burlica R, Shih K Y and Locke B R 2010 Formation of H_2 and H_2O_2 in a water-spray gliding arc nonthermal plasma reactor *Ind. Eng. Chem. Res.* **49** 6342–9

[34] Marotta E, Ceriani E, Schiorlin M, Ceretta C and Paradisi C 2012 Comparison of the rates of phenol advanced oxidation in deionized and tap water within a dielectric barrier discharge reactor *Water Res.* **46** 6239–46

[35] Kovačević V V, Dojčinović B P, Jović M, Roglić G M, Obradović B M and Kuraica M M 2017 Measurement of reactive species generated by dielectric barrier discharge in direct contact with water in different atmospheres *J. Phys. D: Appl. Phys.* **50** 155205

[36] Höft H, Kettlitz M and Brandenburg R 2021 The role of a dielectric barrier in single-filament discharge over a water surface *J. Appl. Phys.* **129** 043301

[37] He B *et al* 2017 Simultaneous quantification of aqueous peroxide, nitrate, and nitrite during the plasma-liquid interactions by derivative absorption spectrophotometry *J. Phys. D: Appl. Phys.* **50** 445207

[38] Oehmigen K, Winter J, Hähnel M, Wilke C, Brandenburg R, Weltmann K D and Von Woedtke T 2011 Estimation of possible mechanisms of Escherichia coli inactivation by plasma treated sodium chloride solution *Plasma Process. Polym.* **8** 904–13

[39] Pavlovich M J, Chang H W, Sakiyama Y, Clark D S and Graves D B 2013 Ozone correlates with antibacterial effects from indirect air dielectric barrier discharge treatment of water *J. Phys. D: Appl. Phys.* **46** 145202

[40] Luo J Y, Nie L L, Liu D W and Lu X 2023 Electrodeless discharge in water: reactive species in liquid and gas phase and energy cost for nitrogen fixation *Plasma Process. Polym.* **20** 2200181

[41] Brandenburg R 2017 Dielectric barrier discharges: progress on plasma sources and on the understanding of regimes and single filaments *Plasma Sources Sci. Technol.* **26** 053001

[42] Lu X, Fang Z, Dai D, Shao T, Liu F, Zhang C, Liu D, Nie L and Jiang C 2023 On the chronological understanding of the homogeneous dielectric barrier discharge *High Volt.* **8** 1132–50

[43] Hänsch M A C, Winter J, Bussiahn R, Weltmann K D and von Woedtke T 2013 A systematic characterization of a novel surface dielectric barrier discharge for biomedical experiments *Plasma Med.* **3** 27–44

[44] Allabakshi S M, Srikar P S N S R, Gangwar R K and Maliyekkal S M 2022 Feasibility of surface dielectric barrier discharge in wastewater treatment: spectroscopic modeling, diagnostic, and dye mineralization *Sep. Purif. Technol.* **296** 121344

[45] Abdelaziz A A, Ishijima T, Osawa N and Seto T 2019 Quantitative analysis of ozone and nitrogen oxides produced by a low power miniaturized surface dielectric barrier discharge: effect of oxygen content and humidity level *Plasma Chem. Plasma Process.* **39** 165–85

[46] Xu H, Zhu F, Liu Y, Quan L, Li B, Zhang H, Shao M and Xie K 2022 Effects of the ground-electrode temperature on the plasma physicochemical processes and biological inactivation functions involved in surface dielectric barrier discharge *Plasma Sources Sci. Technol.* **31** 115010

[47] Boonyawan D, Lamasai K, Umongno C, Rattanatabtimtong S, Yu L D, Kuensaen C, Maitip J and Thana P 2022 Surface dielectric barrier discharge plasma–treated pork cut parts: bactericidal efficacy and physiochemical characteristics *Heliyon* **8** e10915

[48] Galmiz O, Pavliňák D, Zemánek M, Brablec A and Černák M 2017 Hydrophilization of outer and inner surfaces of poly(vinyl chloride) tubes using surface dielectric barrier discharges generated in ambient air plasma *Plasma Process. Polym.* **14** 1600220

[49] Pavliňák D, Galmiz O, Zemánek M, Brablec A, Čech J and Černák M 2014 Permanent hydrophilization of outer and inner surfaces of polytetrafluoroethylene tubes using ambient air plasma generated by surface dielectric barrier discharges *Appl. Phys. Lett.* **105** 154102

[50] Pekárek S 2013 Asymmetric properties and ozone production of surface dielectric barrier discharge with different electrode configurations *Eur. Phys. J.* D **67** 1–7

[51] Pekarek S 2012 Experimental study of surface dielectric barrier discharge in air and its ozone production *J. Phys. D: Appl. Phys.* **45** 075201

[52] Malik M A, Schoenbach K H and Heller R 2014 Coupled surface dielectric barrier discharge reactor-ozone synthesis and nitric oxide conversion from air *Chem. Eng. J.* **256** 222–9

[53] Jeon J, Klaempfl T G, Zimmermann J L, Morfill G E and Shimizu T 2014 Sporicidal properties from surface micro-discharge plasma under different plasma conditions at different humidities *New J. Phys.* **16** 103007

[54] Jeon J, Rosentreter T M, Li Y, Isbary G, Thomas H M, Zimmermann J L, Morfill G E and Shimizu T 2014 Bactericidal agents produced by surface micro-discharge (SMD) plasma by controlling gas compositions *Plasma Process. Polym.* **11** 426–36

[55] Cvetanović N, Galmiz O, Synek P, Zemánek M, Brablec A and Hoder T 2018 Electron density in surface barrier discharge emerging at argon/water interface: quantification for streamers and leaders *Plasma Sources Sci. Technol.* **27** 025002

[56] Galmiz O, Pavlinak D, Zemanek M, Brablec A and Cernak M 2016 Study of surface dielectric barrier discharge generated using liquid electrodes in different gases *J. Phys. D: Appl. Phys.* **49** 065201

[57] Cimerman R, Mat'aš E, Sárený M and Hensel K 2022 Electrical and optical characterization of multi-hollow surface dielectric barrier discharge in configuration with the air-exposed electrode *Phys. Plasmas* **29** 113510

[58] Machala Z, Tarabová B, Sersenová D, Janda M and Hensel K 2019 Chemical and antibacterial effects of plasma activated water: correlation with gaseous and aqueous reactive oxygen and nitrogen species, plasma sources and air flow conditions *J. Phys. D: Appl. Phys.* **52** 034002

[59] Janda M, Hensel K, Tóth P, Hassan M E and Machala Z 2021 The role of HNO_2 in the generation of plasma-activated water by air transient spark discharge *Appl. Sci.* **11** 7053

[60] Keller-Rudek H, Moortgat G K, Sander R and Sörensen R 2013 The MPI-Mainz UV/VIS spectral atlas of gaseous molecules of atmospheric interest *Earth Syst. Sci. Data* **5** 365–73

[61] Jablonowski H and von Woedtke T 2015 Research on plasma medicine-relevant plasma–liquid interaction: what happened in the past five years? *Clin. Plasma Med.* **3** 42–52

[62] Bader H and Hoigné J 1981 Determination of ozone in water by the indigo method *Water Res.* **15** 449–56

[63] Tarabová B, Lukeš P, Janda M, Hensel K, Šikurová L and Machala Z 2018 Specificity of detection methods of nitrites and ozone in aqueous solutions activated by air plasma *Plasma Process. Polym.* **15** 1800030

[64] Eisenberg G M 1943 Colorimetric determination of hydrogen peroxide *Ind. Eng. Chem.* **15** 327–8

[65] Griess P 1879 Bemerkungen zu der Abhandlung der HH. Weselsky und Benedikt „Ueber einige Azoverbindungen" *Ber. Dtsch. Chem. Ges.* **12** 426–8

[66] Moorcroft M J, Davis J and Compton R G 2001 Detection and determination of nitrate and nitrite: a review *Talanta* **54** 785–803

[67] Veronico V, Favia P, Fracassi F, Gristina R and Sardella E 2021 Validation of colorimetric assays for hydrogen peroxide, nitrate and nitrite ions in complex plasma-treated water solutions *Plasma Process. Polym.* **18** 2100062

[68] Kawasaki T, Kusumegi S, Kudo A, Sakanoshita T, Tsurumaru T, Sato A, Uchida G, Koga K and Shiratani M 2016 Effects of irradiation distance on supply of reactive oxygen species to the bottom of a Petri dish filled with liquid by an atmospheric O_2/He plasma jet *J. Appl. Phys.* **119** 173301

[69] Moreau E, Louste C and Touchard G 2008 Electric wind induced by sliding discharge in air at atmospheric pressure *J. Electrostat.* **66** 107–14

[70] Grosch H, Hoder T, Weltmann K D and Brandenburg R 2010 Spatio-temporal development of microdischarges in a surface barrier discharge arrangement in air at atmospheric pressure *Eur. Phys. J.* D **60** 547–53

[71] Allegraud K, Guaitella O and Rousseau A 2007 Spatio-temporal breakdown in surface DBDs: evidence of collective effect *J. Phys. D: Appl. Phys.* **40** 7698–706

[72] Akishev Y, Aponin G, Balakirev A, Grushin M, Karalnik V, Petryakov A and Trushkin N 2013 Spatial–temporal development of a plasma sheet in a surface dielectric barrier discharge powered by a step voltage of moderate duration *Plasma Sources Sci. Technol.* **22** 015004

[73] Akishev Y, Aponin G, Balakirev A, Grushin M, Petryakov A, Karal'nik V and Trushkin N 2013 Stepwise expansion of a surface dielectric barrier discharge as a result of alternation in formation of streamers and leaders *J. Phys. D: Appl. Phys.* **46** 135204

[74] Kossyi I A, Kostinsky A Y, Matveyev A A and Silakov V P 1992 Kinetic scheme of the non-equilibrium discharge in nitrogen-oxygen mixtures *Plasma Sources Sci. Technol.* **1** 207

[75] Kim H-H *et al* 2023 Revisiting why DBDs can generate O_3 against the thermodynamic limit *Int. J. Plasma Environ. Sci. Technol.* **17** 2004–24

[76] Kogelschatz U, Eliasson B and Hirth M 1988 Ozone generation from oxygen and air: discharge physics and reaction mechanisms *Ozone Sci. Eng.* **10** 367–77

[77] Fan X, Kang S, Li J and Zhu T 2018 Formation of nitrogen oxides (N_2O, NO, and NO_2) in typical plasma and plasma-catalytic processes for air pollution control *Water Air Soil Pollut.* **229** 1–12

[78] Pawłat J, Terebun P, Kwiatkowski M, Tarabová B, Kovaľová Z, Kučerová K, Machala Z, Janda M and Hensel K 2019 Evaluation of oxidative species in gaseous and liquid phase generated by mini-gliding arc discharge *Plasma Chem. Plasma Process.* **39** 627–42

[79] Eliasson B and Kogelschatz U 1991 Modeling and applications of silent discharge plasmas *IEEE Trans. Plasma Sci.* **19** 309–23

[80] Teodoru S, Kusano Y and Bogaerts A 2012 The effect of O_2 in a humid $O_2/N_2/NO_x$ gas mixture on NO_x and N_2O remediation by an atmospheric pressure dielectric barrier discharge *Plasma Process. Polym.* **9** 652–89

[81] Kogelschatz U and Baessler P 1987 Determination of nitrous oxide and dinitrogen pentoxide concentrations in the output of air-fed ozone generators of high power density *Ozone Sci. Eng.* **9** 195–206

[82] Shimizu T, Sakiyama Y, Graves D B, Zimmermann J L and Morfill G E 2012 The dynamics of ozone generation and mode transition in air surface micro-discharge plasma at atmospheric pressure *New J. Phys.* **14** 103028

[83] Abdelaziz A A, Ishijima T, Seto T, Osawa N, Wedaa H and Otani Y 2016 Characterization of surface dielectric barrier discharge influenced by intermediate frequency for ozone production *Plasma Sources Sci. Technol.* **25** 035012

[84] Parvulescu V I, Magureanu M and Lukes P 2012 Plasma chemistry and catalysis in gases and liquids *Plasma Chemistry and Catalysis in Gases and Liquids* (Wiley)

[85] Oehmigen K, Hähnel M, Brandenburg R, Wilke C, Weltmann K D and Von Woedtke T 2010 The role of acidification for antimicrobial activity of atmospheric pressure plasma in liquids *Plasma Process. Polym.* **7** 250–7

[86] Dascalu A, Pohoata V, Shimizu K and Sirghi L 2021 Molecular species generated by surface dielectric barrier discharge micro-plasma in small chambers enclosing atmospheric air and water samples *Plasma Chem. Plasma Process.* **41** 389–408

[87] Cimerman R and Hensel K 2023 Multi-hollow surface dielectric barrier discharge: production of gaseous species under various air flow rates and relative humidities *Plasma Chem. Plasma Process.* **43** 1411–33

[88] Kim H Y, Kang S K, Kwon H C, Lee H W and Lee J K 2013 Gas temperature effect on reactive species generation from the atmospheric pressure air plasma *Plasma Process. Polym.* **10** 686–97

[89] Jodzis S 2011 Application of technical kinetics for macroscopic analysis of ozone synthesis process *Ind. Eng. Chem. Res.* **50** 6053–60

[90] Benson S W and Axworthy A E 1957 Mechanism of the gas phase, thermal decomposition of ozone *J. Chem. Phys.* **26** 1718–26

[91] Itoh H, Taguchi M and Suzuki S 2020 Thermal decomposition of ozone at high temperature leading to ozone zero phenomena *J. Phys. D: Appl. Phys.* **53** 185206

[92] Buogo S, Plocek J and Vokurka K 2009 Efficiency of energy conversion in underwater spark discharges and associated bubble oscillations: experimental results *Acta Acust. United Acust.* **95** 46–59

[93] Zhang X, Lee B J, Im H G and Cha M S 2016 Ozone production with dielectric barrier discharge: effects of power source and humidity *IEEE Trans. Plasma Sci.* **44** 2288–96

[94] Chen J and Wang P 2005 Effect of relative humidity on electron distribution and ozone production by DC coronas in air *IEEE Trans. Plasma Sci.* **33** 808–12

[95] Ono R and Oda T 2003 Dynamics of ozone and OH radicals generated by pulsed corona discharge in humid-air flow reactor measured by laser spectroscopy *J. Appl. Phys.* **93** 5876–82

[96] Lukes P, Clupek M, Babicky V, Janda V and Sunka P 2005 Generation of ozone by pulsed corona discharge over water surface in hybrid gas–liquid electrical discharge reactor *J. Phys. D: Appl. Phys.* **38** 409

[97] Van Gaens W and Bogaerts A 2014 Reaction pathways of biomedically active species in an Ar plasma jet *Plasma Sources Sci. Technol.* **23** 035015

[98] Šimek M and Člupek M 2002 Efficiency of ozone production by pulsed positive corona dischargein synthetic air *J. Phys. D: Appl. Phys.* **35** 1171

[99] Samaranayake W J M, Miyahara Y, Namihira T, Katsuki S, Sakugawa T, Hackam R and Akiyama H 2000 Pulsed streamer discharge characteristics of ozone production in dry air *IEEE Trans. Dielectr. Electr. Insul.* **7** 254–60

[100] Judée F, Simon S, Bailly C and Dufour T 2018 Plasma-activation of tap water using DBD for agronomy applications: identification and quantification of long lifetime chemical species and production/consumption mechanisms *Water Res.* **133** 47–59

[101] Yang J K, Cho C H, Kim J H, Seok D C, Yoo S and Kang I J 2022 Water surface plasma source for large area water treatment by using volume dielectric barrier discharge *IEEE Trans. Plasma Sci.* **50** 4612–9

[102] Hoeben W F L M, van Ooij P P, Schram D C, Huiskamp T, Pemen A J M and Lukeš P 2019 On the possibilities of straightforward characterization of plasma activated water *Plasma Chem. Plasma Process.* **39** 597–626

[103] Xiao A, Liu D, Li Y, Xiao A, Liu D and Li Y 2023 Plasma-activated tap water production and its application in atomization disinfection *Appl. Sci.* **13** 3015

[104] Chiappim W, Sampaio A D G, Miranda F, Fraga M, Petraconi G, da Silva Sobrinho A, Kostov K, Koga-Ito C and Pessoa R 2021 Antimicrobial effect of plasma-activated tap water on Staphylococcus aureus, Escherichia coli, and Candida albicans *Water* **13** 1480

[105] Kooshki S, Pareek P, Mentheour R, Janda M and Machala Z 2023 Efficient treatment of bio-contaminated wastewater using plasma technology for its reuse in sustainable agriculture *Environ. Technol. Innov.* **32** 103287

[106] Oehmigen K, Hoder T, Wilke C, Brandenburg R, Hahnel M, Weltmann K D and Von Woedtke T 2011 Volume effects of atmospheric-pressure plasma in liquids *IEEE Trans. Plasma Sci.* **39** 2646–7

[107] Rumbach P, Griggs N, Sankaran R M and Go D B 2014 Visualization of electrolytic reactions at a plasma-liquid interface *IEEE Trans. Plasma Sci.* **42** 2610–1

[108] Hassan M E, Janda M and Machala Z 2021 Transport of gaseous hydrogen peroxide and ozone into bulk water vs electrosprayed aerosol *Water* **13** 182

[109] Itikawa Y and Mason N 2005 Cross sections for electron collisions with water molecules *J. Phys. Chem. Ref. Data* **34** 1–22

[110] Sieck L W, Herron J T and Green D S 2000 Chemical kinetics database and predictive schemes for humid air plasma chemistry. Part I: positive ion—molecule reactions *Plasma Chem. Plasma Process.* **20** 235–58

[111] Attri P, Kim Y H, Park D H, Park J H, Hong Y J, Uhm H S, Kim K N, Fridman A and Choi E H 2015 Generation mechanism of hydroxyl radical species and its lifetime prediction during the plasma-initiated ultraviolet (UV) photolysis *Sci. Rep.* **5** 1–8

[112] Tian W and Kushner M J 2014 Atmospheric pressure dielectric barrier discharges interacting with liquid covered tissue *J. Phys. D: Appl. Phys.* **47** 165201

[113] Vilema-Enríquez G, Arroyo A, Grijalva M, Amador-Zafra R I and Camacho J 2016 Molecular and cellular effects of hydrogen peroxide on human lung cancer cells: potential therapeutic implications *Oxid. Med. Cell. Longev.* **2016** 1908164

[114] Boehm D, Curtin J, Cullen P J and Bourke P 2017 Hydrogen peroxide and beyond-the potential of high-voltage plasma-activated liquids against cancerous cells *Anti Cancer Agents Med. Chem.* **18** 815–23

[115] Niethammer P, Grabher C, Look A T and Mitchison T J 2009 A tissue-scale gradient of hydrogen peroxide mediates rapid wound detection in zebrafish *Nature* **459** 996–9

[116] Ji S, Ki S H, Kang M H, Choi J S, Park Y, Oh J, Kim S B, Yoo S J, Choi E H and Park G 2018 Characterization of physical and biochemical changes in plasma treated spinach seed during germination *J. Phys. D: Appl. Phys.* **51** 145205

[117] Bafoil M, Jemmat A, Martinez Y, Merbahi N, Eichwald O, Dunand C and Yousfi M 2018 Effects of low temperature plasmas and plasma activated waters on Arabidopsis thaliana germination and growth *PLoS One* **13** e0195512

[118] Bruggeman P and Schram D C 2010 On OH production in water containing atmospheric pressure plasmas *Plasma Sources Sci. Technol.* **19** 045025

[119] Zhao Y Y, Wang T, Wilson M P, MacGregor S J, Timoshkin I V and Ren Q C 2016 Hydroxyl radicals and hydrogen peroxide formation at nonthermal plasma-water interface *IEEE Trans. Plasma Sci.* **44** 2084–91

[120] Ito T, Uchida G, Nakajima A, Takenaka K and Setsuhara Y 2017 Control of reactive oxygen and nitrogen species production in liquid by nonthermal plasma jet with controlled surrounding gas *Jpn. J. Appl. Phys.* **56** 01AC06

[121] Stará Z and Krčma F 2004 The study of H_2O_2 generation by DC diaphragm discharge in liquids *Czech. J. Phys.* **54** C1050–5

[122] Zhou R, Zhou R, Zhang X, Zhuang J, Yang S, Bazaka K and Ostrikov K K 2016 Effects of atmospheric-pressure N_2, He, air, and O_2 microplasmas on mung bean seed germination and seedling growth *Sci. Rep.* **6** 1–11

[123] Girard F, Badets V, Blanc S, Gazeli K, Marlin L, Authier L, Svarnas P, Sojic N, Clément F and Arbault S 2016 Formation of reactive nitrogen species including peroxynitrite in physiological buffer exposed to cold atmospheric plasma *RSC Adv.* **6** 78457–67

[124] Neretti G, Taglioli M, Colonna G and Borghi C A 2016 Characterization of a dielectric barrier discharge in contact with liquid and producing a plasma activated water *Plasma Sources Sci. Technol.* **26** 015013

[125] Park J Y, Park S, Choe W, Yong H I, Jo C and Kim K 2017 Plasma-functionalized solution: a potent antimicrobial agent for biomedical applications from antibacterial therapeutics to biomaterial surface engineering *ACS Appl. Mater. Interfaces* **9** 43470–7

[126] Hansch M A C, Mann M, Weltmann K D and Von Woedtke T 2015 Analysis of antibacterial efficacy of plasma-treated sodium chloride solutions *J. Phys. D: Appl. Phys.* **48** 454001